Waveguide-Thru Closed-Form Characterization of Anisotropic Polymer Network Liquid-Crystal for mmWave Reconfigurable RF Devices

Hogyeom Kim, *Graduate Student Member, IEEE*, Jae-Won Lee, *Graduate Student Member, IEEE*,
Junkai Wang, *Graduate Student Member, IEEE*, Min-Seok Kim, *Student Member, IEEE*,
Hak-Rin Kim, *Member, IEEE*, and Jungsuek Oh, *Senior Member, IEEE*

Abstract— In this article, closed-form characterization of anisotropic polymer network liquid-crystal (PNLC) for reconfigurable RF devices at the millimeter-wave (mmWave) band is achieved. For the first time, the complex permittivity of the PNLC has been extracted for various doping conditions of reactive mesogen used in the polymer network at the mmWave band. Anisotropic constitutive parameters at the two extreme states of the PNLC can be obtained through a waveguide (WG). A 1 × 2 reflectarray simple cell in the WG enables the establishment of an equivalent circuit (EQ) for an infinite cell array, providing exact modeling for de-embedding. The PNLC has an attractive property compared with pristine nematic liquid crystals (NLCs) owing to its significantly enhanced dynamic switching characteristics. In the mmWave band, the physical cell gap of the liquid crystal (LC) inevitably increases to achieve RF performance, resulting in slow dynamic speed. However, studies on the characterization of PNLCs at the mmWave band are limited, and their evaluation methodologies are inaccurate. The fabricated cell requires no biasing circuit to achieve two extreme phase states, owing to its prealigned layer. With the proposed novel method, constitutive parameters of other LC types, modified by doping approaches for RF performance can be precisely extracted and predicted.

Index Terms— Dynamic switching time, liquid crystal (LC), polymer network liquid crystal (PNLC), reactive mesogen.

I. INTRODUCTION

LIQUID crystal (LC)-based reconfigurable RF devices, such as phase shifters and antennas, are electronically controllable devices with beam scanning ability to achieve wide beam coverage [1], [2], [3], [4], [5], [6], [7], [8]. In particular, LCs have been employed in reconfigurable antenna (RA) designs to replace phase shifters and to reduce complexity. Among the several reconfigurable components, such as p-i-n diodes, varactor diodes, and MEMS switches, LC-based devices have distinctive advantages. Power consumption and heat emissions are almost zero because a low current is generated in the biasing backplane circuit. Moreover, the quantization error in RAs is significantly lower than that in other reconfigurable component-based RAs, owing to their continuous dynamic phase range according to the applied bias voltage level. The most noteworthy advantages of LC are the operating frequency band and the cost associated with manufacturing a large-scale aperture. LCs have reliable characteristics over a broad frequency range, from the microwave to the optical band, to operate RA [9], [10], [11]. In addition, a positive trend exists in which, with an increase in frequency, the required amount of LC can be significantly decreased because of the much reducible LC-RA thickness and electrically switchable array scale. As future devices toward the sub-THz band, the need to commercialize LC-RA technologies is gradually increasing.

Several studies to determine the functionalities of LC-RAs in the millimeter wave (mmWave) band have been conducted [12], [13], [14], [15], [16]. Most LC-RAs comprise pure nematic LCs (NLCs), which have high dielectric anisotropies and low loss factors and exhibit remarkable performances. However, the viscosity of the LC influences its slow speed and the NLC layer requires a physically thick cell gap, compared with optical applications, to generate RF band resonance, resulting in slow switching times of up to tens of seconds, particularly for the field-off response.

Recently, polymer network LC (PNLC)-based RA has been developed to enhance the dynamic switching characteristics in the mmWave band [17], [18]. PNLCs comprised pure NLC mixed with reactive mesogens (RMs). The LC layer stabilized by the RM-distributed networks is formed through an ultraviolet (UV)-curing post-process. Owing to LC anchoring effects at RM networks distributed within the LC bulk and significantly reduced effective LC cavity effects, the switching dynamics of LC-based RF antennas can be effectively improved. Compared with field-driven switching dynamics,

field-off switching dynamics are expected to be considerably improved because the LC director recovery dynamics are governed by the LC anchoring properties at the boundary surfaces. However, phase and amplitude responses should be predesigned based on permittivity for efficient RA based on accurate electrical properties; therefore, any modifications to the LC complicate the systematic design owing to unknown material parameters. Moreover, the PNLC is extremely challenging to establish because of their delicate fabrication, such as monomer combinations or mixtures and particle composition.

In [17], the first trial on the characterization of PNLC at mmWave frequencies was conducted. However, the electrodes of the PNLC structure in [17] comprised 1 μm thick gold that was not optically transparent. One side of the electrode must be optically transparent and properly polymerized by UV exposure to form an appropriate PNLC network. In addition, a 20 wt% concentration level was applied to construct the PNLC, which showed low LC anisotropy and a high loss factor [17], which is not compatible with the antenna. To operate an RA with the desired performance, the LC cavity should be doped with an appropriate amount of RM. Because of the complex quasi-static field distribution, LC characterization should be performed in a sophisticated manner to employ the permittivity tensor in the RF domain. Some studies have characterized LC in the field of RF [17], [18], [19], [20], [21]. In [17], when biased, the complex unit cell structure influenced the permittivity tensor, making it challenging to extract the exact permittivity of the LC. In [18], a circular patch resonator with a high-quality factor was employed to characterize LC permittivity. The scalar permittivity was obtained by matching the operating frequencies. Although an iterative process was conducted, errors occurred in the bias lines, radiation, and supporting dielectrics. In [19], an LC-based reflectarray in the sub-THz band was tested, and its anisotropy was validated from the phase shift range but without a closed-form solution. In [20] and [21], broadband measurements of the effective permittivity and loss tangent were successfully achieved through a thrust de-embedding method by utilizing a multilayered microstrip structure. However, the proposed structures for characterization were quite complex, leading to extraction errors owing to fabrication errors and complex field distributions caused by the electrodes.

In this study, a waveguide (WG)-through closed-form characterization of anisotropic materials, including permittivity and loss tangents, was achieved. There is no study on the characterization of complex permittivity at the mmWave band. The proposed method is cost-effective because of its simple unit cell structure and measurement process. The fabricated unit cell requires no biasing system due to its prealigned layer, which enables the establishment of two extreme phase states. Additionally, transparent electrodes achieve various concentrations of the RM through UV exposure. Fabrication and measurement errors can be significantly reduced without establishing a bulky and complex array structure comprising numerous unit LC cells. Owing to the operating principle of the unit cell, the two extreme states of anisotropic materials can be extracted with high accuracy by introducing an

equivalent circuit (EQ) for de-embedding. The operation mode of the 1 × 2 cell is predominantly influenced by the z-component of the LC due to its TM mode [37]. Through this mechanism, the unknown properties of anisotropic LC material can be determined. The PNLC was chosen in this study to demonstrate the proposed WG method as a solution to significantly enhance the switching dynamics of the LC, but unknown for employing the characteristics. In addition, by utilizing the proposed extraction method, the constitutive parameters of other types of LC candidates modified by doping approaches for the RF performance can be precisely predicted. By simply changing the cell dimensions and WG, the desired frequency band can be easily characterized. PNLC-based 1×2 reflectarray cells were designed with various RM doping concentrations ranging from 0 to 8 wt%, and, finally, the optimal doping condition was determined by measuring and comparing the transmittance, switching time, and bias voltage level. WR28 was employed to obtain the effective permittivity and loss tangent of the mixture. This result was validated by comparing the full-wave simulation and measurement results.

The remainder of this article is organized as follows. Section II presents the basic characteristics of LC and an introduction to the extraction method for the characterization of PNLC. Section III discusses the fabrication process and the measurement results. Finally, Section IV concludes this article.

II. PRELIMINARIES

A. Characteristics of the Pristine LC and PNLC

This section discusses the principles of pristine and PNLC in detail. Schematics of field-driven LC reorientations of pristine LCs anchored by LC alignment layers formed at two boundary surfaces and PNLCs anchored by RM networks bulk-distributed within the LC layer are shown in Fig. 1. Because of the LC dielectric anisotropy when an electric field is applied, the rod-like LC molecules are field-driven and reoriented along the applied field direction with competition owing to the LC elastic effects. The effective permittivity of the uniaxial tensor shown in Fig. 1(a) is expressed as follows:

$$\overline{\overline{\varepsilon_r}}\,(\bar{r}) = \varepsilon_{r\perp}\bar{I} + \varepsilon_{r\perp}\bar{I}\Delta\varepsilon_r\bar{N}\,(\bar{r}) \tag{1}$$

where $\overline{\overline{I}}$ is the second-order identity tensor, $\Delta\varepsilon_r = \varepsilon_\parallel - \varepsilon_\perp$ is the dielectric anisotropy of the LC, and $\overline{\overline{N}} = \hat{n}(\bar{r})\otimes\hat{n}(\bar{r})$ is the second-order tensor. $\hat{n}(\bar{r})$ is a unit vector that is macroscopically defined by the average direction of the local molecules. When the bias voltage is applied, the NLC director vector $\hat{n}(\bar{r})$ rotates, causing the permittivity distribution to vary. Notably, electrostatic energy is converted into elastic energy when the external quasi-static field E_b excites the LC cavity [22]. This energy, called the Frank-Oseen elastic and electrostatic free energy, is minimized such that vector $\hat{n}$ varies. The elastic f_D and electrostatic f_E free energy densities were derived using the following equations [23]:

$$f_D = \frac{k_{11}}{2}(\nabla \cdot \hat{n})^2 + \frac{k_{22}}{2}(\hat{n} \cdot \nabla \times \hat{n})^2 + \frac{k_{33}}{2}\left|\hat{n} \times (\nabla \times \hat{n})\right|^2 \tag{2}$$

$$f_E = \frac{1}{2}\varepsilon_0 E_b \cdot \overline{\overline{\varepsilon_r}} \cdot E_b \tag{3}$$

where k_{11}, k_{22}, and k_{33} are the elastic constants related to the splay, twist, and bend LC deformations, respectively. The orientation of the LC can be determined by minimizing the free energy after considering the LC-anchoring surface energy density, as expressed in the following equation:

$$min\,(F) = min\left(\iiint \Omega\,(f_D - f_E)\,d\Omega + \oiint_\Gamma f_S d\Gamma\right) \quad (4)$$

where Ω and Γ are the volume and surface of the cavity, respectively. f_S represents the surface energy density related to LC anchoring at the alignment layers. The field-on (τ_{on}) and field-off (τ_{off}) switching dynamics of the conventional LC devices anchored by two boundary substrates when the strong surface anchoring conditions are assumed at the LC alignment surfaces can be expressed as follows:

$$\tau_{on} = \left(\frac{h}{\pi}\right)^2 \frac{\gamma}{K_{eff}} \left(\frac{1}{(V/V_{th})^2 - 1}\right) \quad (5)$$

$$\tau_{off} = \left(\frac{h}{\pi}\right)^2 \frac{\gamma}{K_{eff}} \quad (6)$$

where h, γ, and K_{eff} represent the LC cell gap, viscosity, and effective elastic constant assuming the one elastic constant approximation, respectively. Viscosity and elastic constant are the LC material characteristics employed in LC devices. $V_{th} = \pi\sqrt{(K_{eff}/(\varepsilon_0 \Delta\varepsilon))}$ represents the Frederiks threshold voltage where the LC directors within the LC cavity start changing at that bias voltage level (V_{th}) in response to an applied field. The larger the anisotropy $\Delta\varepsilon$, the smaller the achievable threshold voltage. The characteristics of τ_{on} can be reduced by decreasing the LC cell gap or increasing the bias voltage level. LC-RAs require a physically thick LC gap to achieve the desired RF performances [24], [25], [26]. In contrast to the τ_{on} property that can be improved by bias voltage designs, the field-off recovery time of τ_{off} suffers from a considerably slow switching time, which should be improved by the LC material itself or LC anchoring condition. These slow-recovery dynamics can be mitigated by doping carbon nanotubes into LCs to enhance LC-LC interactions, employing dual-frequency LCs for field-induced LC recovery, nano-encapsulating LC droplets, or establishing PNLC [17], [27], [28], [29], [30]. PNLCs can be realized by adding a UV-curable RM to the LC cavity, and the LC-anchoring surfaces are distributed as RM networks within the LC bulk after UV-induced RM polymerization. PNLCs have local LC domains, as shown in Fig. 1(b), where the LC domains have different domain gaps according to polymerization conditions, such as RM doping conditions, processing temperature during UV irradiation, and UV dose intensity involving phase-separated polymeric networks. RM networks work strongly as LC-anchoring distributed surfaces, leading to improved dynamics, particularly in field-off switching operations.

Moreover, the polymer network achieved a thin effective cell gap, and the cell gap h_{PNLC}^{eff} of the PNLC was lower than that of the NLC, as expressed in the following equation:

$$h_{PNLC}^{eff} = \frac{1}{N}\sum_1^N h_{PNLC}^n < h_{NLC}. \quad (7)$$
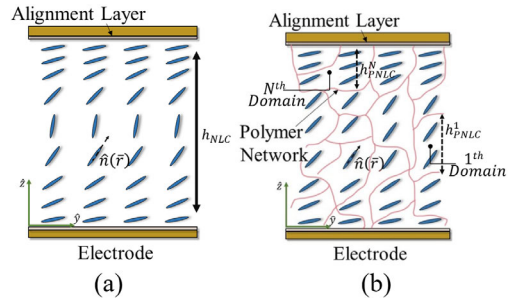

Fig. 1. Schematics of field-driven LC reorientations of (a) pristine LC anchored by LC alignment layers at two boundary substrates and (b) PNLC anchored by RM networks distributed within the LC bulk layer.

However, owing to the LC-distributed RM networks, the essential material parameters in the RF performances of the dielectric anisotropy of the PNLC inevitably decreased, and the loss tangent increased. The doping-modified permittivity of the PNLC can be expressed as follows:

$$\overline{\overline{\varepsilon_{r\perp}}}\bigg|_{V_b < V_{th}} = \begin{pmatrix} \varepsilon_{r\perp} + \beta & 0 & 0 \\ 0 & \varepsilon_{r\parallel} - \alpha & 0 \\ 0 & 0 & \varepsilon_{r\perp} + \beta \end{pmatrix} \quad (8)$$

$$\overline{\overline{\varepsilon_{r\parallel}}}\bigg|_{V_b \gg V_{th}} = \begin{pmatrix} \varepsilon_{r\perp} + \beta & 0 & 0 \\ 0 & \varepsilon_{r\perp} + \beta & 0 \\ 0 & 0 & \varepsilon_{r\parallel} - \alpha \end{pmatrix}. \quad (9)$$

We assumed that the alignment layers were rubbed along the y-axis. The two extreme states change according to the RM doping weight percentage. Equations (8) and (9) are reconstructed uniaxial tensors with correction terms, α and β, from the permittivity of the pristine LC. $\varepsilon_\perp$ at the zero bias state increases by β and the permittivity $\varepsilon_\parallel$ at the full bias state decreases by α. α and β are determined according to the concentration level of the RM within the employed LC-RM mixture. Moreover, the loss tangents of both extreme states increase, as expressed in the following equations:

$$\overline{\overline{tan\delta_\perp}}\bigg|_{V_b < V_{th}} = \begin{pmatrix} tan\delta_\perp + \Delta & 0 & 0 \\ 0 & tan\delta_\parallel + \xi & 0 \\ 0 & 0 & tan\delta_\perp + \Delta \end{pmatrix} \quad (10)$$

$$\overline{\overline{tan\delta_\parallel}}\bigg|_{V_b \gg V_{th}} = \begin{pmatrix} tan\delta_\perp + \Delta & 0 & 0 \\ 0 & tan\delta_\perp + \Delta & 0 \\ 0 & 0 & tan\delta_\parallel + \xi \end{pmatrix} \quad (11)$$

where ξ and Δ represent correction terms for the loss tangent. Contrary to the permittivity, the loss tangent at the two extreme states increased with the addition of the lossy material. Otherwise, the constitutive parameters of the PNLC were assumed to be scalar values [17]. The variation terms α, β, ξ, and Δ in this study are precisely extractable by employing the proposed method with the WG and 1×2 RA cell.

B. Characterization Method Utilizing the 1×2 RA Cell With WR-28 WG

This subsection introduces a characterization method by utilizing a 1×2 RA cell with a WR-28 WG. Although the
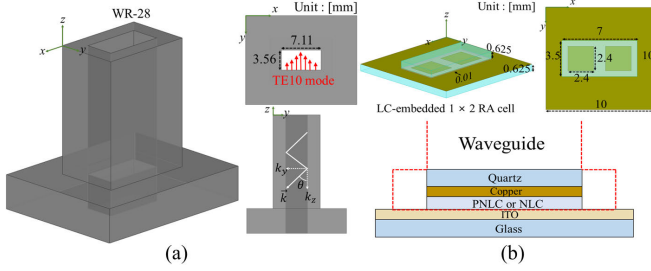
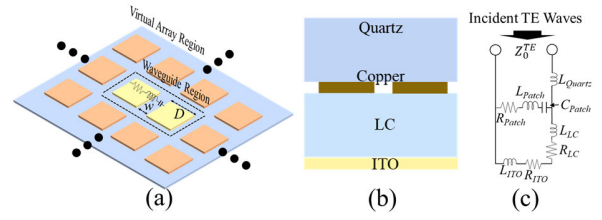Fig. 2. (a) WR-28 WG and (b) LC-embedded 1 × 2 RA cell.

Fig. 3. Periodic array with lumped element and corresponding EQ circuit of the 1 × 2 RA LC cell. (a) Area for the virtual and waveguide region, (b) side view of the 1 × 2 RA cell, and (c) EQ circuit.

WG method is widely known to validate the characteristics of infinite array cells [31], studies on the extraction of the permittivity and loss tangent of modified LC materials, such as the LC-RA device, simultaneously with the de-embedding of the measured results utilizing an EQ circuit are unavailable. The WG extraction method has several advantages, such as ease of de-embedding, low cost of manufacturing the antenna under test (AUT), and high accuracy.

The WR-28 WG and designed LC-embedded 1 × 2 RA cell utilized as the AUT is shown in Fig. 2. As shown in Fig. 2(a), the fundamental TE10 mode was excited to evade over mode. Therefore, the operating frequency range of the WG was chosen from 26.5 to 40 GHz. Although the Ka-band was assumed in this study, the constitutive parameters in other spectra can be easily investigated by choosing the corresponding WGs and adjusting the lateral dimension of the patch and periodicity of the 1 × 2 RA cell to resonate at the desired band. The designed 1 × 2 RA cell utilized to extract the permittivity and loss tangent of the fabricated LC cell is shown in Fig. 2(b). The upper and lower sides of the LC electrodes are made of copper and indium tin oxide (ITO), respectively. The ITO acts as an RF ground and UV ray window to create a UV-induced polymer network in the LC-RM mixture. To provide a uniformly distributed RM network within a 1 × 2 RA cell, the UV-irradiation intensity must be sufficiently strong. Otherwise, the RM network densities are formed in a gradient, where those near the UV irradiation surface are higher owing to RM diffusion during UV-induced phase separation accompanied by UV-induced photo-polymerization. In addition, quartz with a thickness of 0.625 mm provides high optical transparency. To achieve resonance at approximately 35 GHz, the square patch size was chosen as 2.4 × 2.4 mm. The LC cell of 1 × 2 RA cell samples had a cell gap of 10 μm. In this study, five doping weight concentrations of the RM were considered, and the effectiveness of the proposed method was demonstrated by comparing it with a full-wave simulation. Studies on the influence of the doping concentration of the RM on the RF performance and LC dynamics have not been conducted. To extract constitutive parameters, such as permittivity and loss tangent, an EQ circuit should be constructed.

A 1 × 2 RA cell embedded in the WG, where the cells generated by the WG were arranged around the 1 × 2 RA cell is shown in Fig. 3(a). The establishment of the EQ is based on the theory of frequency selective surface [39]. The WG simulator imitates the Floquet simulation with an angle of incidence θ, determined by the cut-off frequency f_c. The

square patch of an infinite array on a lossy medium can be modeled as a series RLC circuit [32]. In addition, low-loss quartz and lossy material were modeled as an inductor and a series RL circuit, respectively, as shown in Fig. 3(b). The corresponding EQ of the 1 × 2 RA RM-modified LC cell in the WG is shown in Fig. 3(c). The semi-infinite free space in the WG is described by the propagation constant k_0. Because the fundamental mode excited the TE10 waves, the characteristic impedance is $Z_0^{TE} = \omega\mu0/k$. The propagation constant k is defined $k = \sqrt{k_0^2 - k_t^2}$, where $k_t = k_0 sin\theta$ is the transverse wavenumber. The angle of incidence was calculated considering the wave propagation number

$$\theta = sin^{-1}\frac{k_t}{k} = sin^{-1}\frac{\lambda_0}{\lambda_c} = sin^{-1}\frac{f_c}{f} \qquad (12)$$

where λ_0 and λ_c are the free space and cut-off wavelengths, respectively. The series inductance and capacitance, related to the metallic patch are modeled as $Z_{Patch} = R_{Patch} + j\omega L_{Patch} - j/\omega C_{Patch}$, considering field distribution and adjacent electrodes [32], [33]

$$C_{Patch} = \varepsilon_0\varepsilon_{eff}\frac{2D}{\pi}log\left(csc\frac{\pi(D-w)}{2D}\right)\left(1 - \frac{k_0^2}{k_{eff}^2}\frac{sin^2\theta}{2}\right) \qquad (13)$$

$k_{eff1} = k_0\sqrt{\varepsilon}_{eff}$ is the effective propagation constant in the effective host medium with effective permittivity ε_{eff} [34]. D and w represent the periodicity and gap of the patch, respectively. The inductance can be efficiently calculated by employing a full-wave simulator [35]. As the metallic patches introduced in this study are printed on thin dielectric, higher-order Floquet mode reflections from the ground plane should be considered [36]

$$C_{mod} = C_{Patch} - \frac{2D\varepsilon_0\varepsilon_{eff}}{\pi}log\left(1 - exp\frac{-4\pi d}{D}\right) \qquad (14)$$

where the LC cell gap is defined as d. This modified capacitance included a reduced patch caused by interlayer coupling. The resistance of the metallic patches adjacent to the LC layer is expressed as

$$R_{Patch} = \frac{-2\varepsilon_{LC}''}{\omega C_{mod}\left(\varepsilon_{LC}''^2 + \varepsilon_{eff}^2 - sin^2\theta\right)}. \qquad (15)$$

ε_{LC}'' represents the imaginary part of the complex permittivity of the LC. The resistance of the series RL circuit is shown in Fig. 3(c), $R_{LC} + jL_{LC}$ can be calculated as expressed
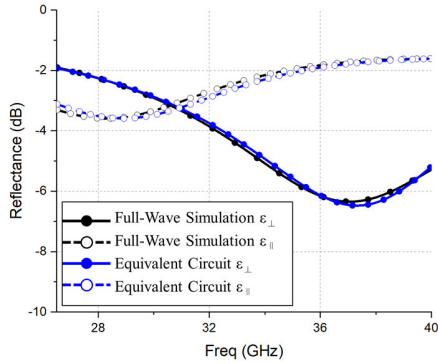
Fig. 4. Frequency response comparison of the LC-embedded 1×2 RA cell between full-wave simulation and EQ circuit model.
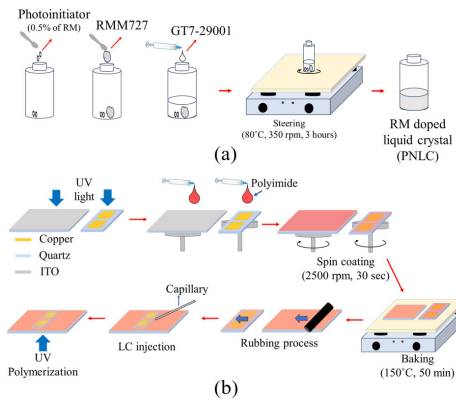

Fig. 5. (a) Fabrication process of the RM-doped LC mixture and (b) 1×2 RA LC cell.

in (16), as shown at the bottom of the next page. A grounded dielectric slab of thickness d is expressed as (17), as shown at the bottom of the next page. $k_2 = k_0 \sqrt{\varepsilon_{eff2}}$ represents the propagation constant for LC. The lossless transmission lines, related to L_{Quartz} is $\mu_0 t_{Quartz}$ where μ_0 and t_{Quartz} represent the free space permeability and thickness of the quartz, respectively.

The S_{11} results from the full-wave simulation and EQ circuit model are shown in Fig. 4. The solid and dashed lines represent two extreme states of the LC, $\varepsilon_\perp$, and $\varepsilon_\parallel$, respectively. The black and blue lines represent the full-wave simulation and EQ circuit results, respectively, as calculated using MATLAB. In the simulation, the relative permittivity of the LC is complex ($\varepsilon'_{LC} - j\varepsilon''_{LC}$) owing to its loss feature. A GT7 LC (Merck KGaA, Darmstadt, Germany) was utilized in this study. Based on the datasheet, the tunable range of the dielectric constant of the LC adopted here was expected to be 2.46–3.56 (from $\varepsilon_\perp$ to $\varepsilon_\parallel$ at 19 GHz). The corresponding loss tangent decreased from 0.012 to 0.0064. The dielectric constant and loss tangent of the quartz were 3.9 and 0.0004, respectively. In addition, the thickness of the copper and ITO electrodes were chosen as 15 μm and 150 nm, respectively. The sheet resistance and inductance of the ITO were 12 Ω/sq, respectively. The simulation results were related to two extreme states of the LC, and the results were obtained by utilizing ANSYS HFSS. Owing to the operating principle of the unit cells, the z-component of the permittivity tensor predominantly influenced the performance of the unit cell [37], [38]. The permittivity of the LC in the full-wave simulation

was assumed to be a uniaxial tensor with an EQ model scalar value. The reflection coefficient Γ of the EQ circuit model in Fig. 4 was calculated as expressed in the following equation:

$$\Gamma = \frac{Z_{in} - \omega\mu_0/\sqrt{k_0^2 - k_t^2}}{Z_{in} + \omega\mu_0/\sqrt{k_0^2 - k_t^2}} \tag{18}$$

where Z_{in} represents the input impedance of the 1×2 RA LC cell.

III. CHARACTERIZATION RESULTS OF THE PNLC

A. Fabrication Process

This section introduces the fabrication process of PNLC-embedded 1×2 RA cells. The detailed fabrication process utilized to prepare a well-dispersed RM-doped LC mixture is shown in Fig. 5(a). The RM-doped LC mixture comprised a photoinitiator (Irgacure 651, Ciba Specialty Chemicals), RM (RMM 727, Merck KGaA, Darmstadt, Germany), and LC (GT7-29001, Merck KGaA, Darmstadt, Germany). The radical-generating photoinitiator was added in an amount of 0.5 wt% of the LC-RM mixture to promote the uniform RM network distribution at the UV-induced photo-polymerization and phase separation step by the enhanced UV reaction rate. RM molecules have LC-like molecular structures and are well mixed with the LC host. In our experiment, to obtain a better homogeneous solution, the homogenizing agitation process was additionally performed by utilizing a hot plate magnetic stirrer at an elevated temperature condition of approximately 80 °C at 350 r/min for more than 3 h.

The detailed fabrication process of the 1×2 RA LC cell is shown in Fig. 5(b) as follows:

1) For surface cleaning, UV ozone surface treatment was performed on both quartz and glass substrates, which also improved the surface coating properties by modifying the surface to be hydrophilic. The thickness of the 1×2 copper pattern, deposited to the quartz substrate, and the ITO common electrode, deposited to the glass substrate, were 15 μm and 150 nm, respectively.

2) Two types of polyimide (PI) solution were chosen for two extreme states to promote azimuthal or polar LC orientations at the surfaces, and one of them was spin-coated, for each cell, onto both electrode-formed substrates at 2500 r/min to form an LC alignment layer. Subsequently, heat treatment was performed at 150 °C for approximately 50 min to remove the solvent and to provide the PI polymerization.

3) An antiparallel rubbing process was performed on LC alignment PI layers, and the rubbing direction was set to be parallel to the direction of the electric field in the dominant mode of the WR 28 WG.

4) Quartz and glass substrates with the rubbed PI layers were assembled with a uniform cell gap ($\sim$10 μm) by utilizing sealant-mixed spacers. The empty cells were placed on a hot plate heated above the phase transition temperature of the RM-doped LC mixtures; subsequently, the LC-RM mixture was capillary injected and the device side edges were sealed.
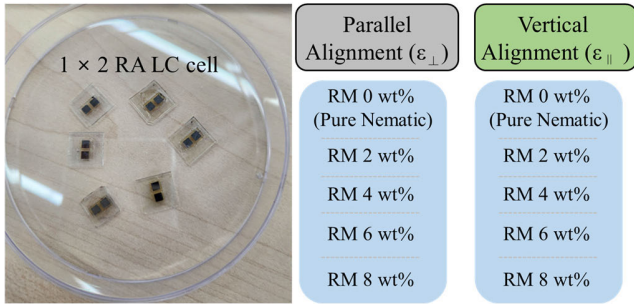
Fig. 6. Fabricated samples of the 1×2 RA LC cell.
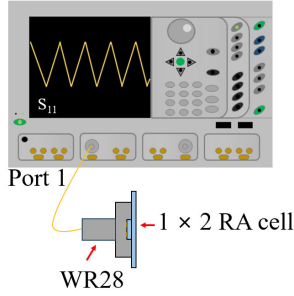

Fig. 7. Measurement setup of the 1×2 RA LC cell for RF extraction.

5) Finally, to form well-dispersed RM networks within the LC cavity, UV was irradiated for 30 min toward the ITO-deposited glass substrate. Several types of 1×2 RA LC cells were fabricated, as shown in Fig. 6, by varying the RM concentration, with five RM concentrations ranging from 0 to 8 wt%. The prepared 1×2 RA LC samples were characterized by utilizing a WR 28 WG.

B. RF Characterization

The measurement setup utilized to evaluate the 1×2 RA LC cell in terms of RF is shown in Fig. 7. In the RF test, the WG WR28 was employed, where the S_{11} parameter was measured by utilizing a vector network analyzer (VNA) after embedding the cell into the WR28 WG, which was connected to port 1. The MS4647A VNA from Anritsu was utilized in this study.

De-embedding was performed after the S_{11} parameter results were measured by employing the EQ model, and the permittivity, as well as loss tangent, can then be extracted. In this study, two types of LC alignment PIs were employed to investigate the RM-dependent uniaxial dielectric properties
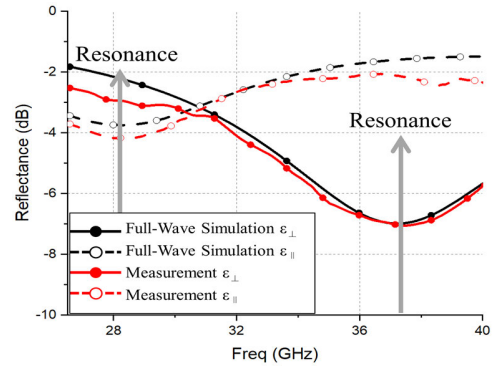

Fig. 8. Comparison between simulation results and measured results of pure NLC (RM 0 wt%).

of RM-stabilized LC cells: homeotropic and homogeneously planar LC-aligned PIs.

A comparison between the full-wave simulation results and measured results of the pure NLC (0 wt% RM condition) is shown in Fig. 8. The solid and dashed lines represent two extreme states of the LC, $\varepsilon_\perp$, and $\varepsilon_\parallel$, respectively. The black and red lines represent the full-wave simulation and measured results from the VNA, respectively. Because the EQ results match the full-wave simulation, the de-embedding of the measured results can be processed by utilizing the EQ model. The constitutive parameters were extracted near the resonance point because the impedance changed significantly, and the equation guaranteed fidelity at resonance

$$\varepsilon_{eff} \underset{V_b < V_{th}}{\triangleq} \varepsilon_{r\perp} + \beta \tag{19}$$

$$\varepsilon_{eff} \underset{V_b >> V_{th}}{\triangleq} \varepsilon_{r\parallel} - \alpha \tag{20}$$

$$tan\delta_{eff} \underset{V_b < V_{th}}{\triangleq} tan\delta_\perp + \Delta \tag{21}$$

$$tan\delta_{eff} \underset{V_b >> V_{th}}{\triangleq} tan\delta_\parallel + \xi. \tag{22}$$

Because of the fundamental field distribution in the unit cell, the constitutive parameters of the two extreme states could be extracted by assuming them to be scalar values, as expressed in (19)–(22). Thus, the four meaningful correction terms of α, β, Δ, and ξ were calculated, as summarized in Table I.

The measured S_{11} results versus the RM weight percentage ranging from 0 to 8 wt% are shown in Fig. 9. To extract the two extreme states, the planar and homeotropic LC alignment cases are shown in Fig. 9(a) and (b), respectively. As shown in Fig. 9(a), the resonance frequencies moved to the left along the x-axis as the RM concentration increased. Thus, when the

$$R_{LC} = \frac{k_2}{\omega\varepsilon_0(\varepsilon'_{LC} - sin^2\theta)^{1/2}} \left[\frac{\varepsilon''_{LC}}{2\left(\varepsilon'_{LC} - sin^2\theta\right)} tan\left(k_2 d \left(\varepsilon'_{LC} - sin^2\theta\right)^{1/2}\right) - h_{LC} \frac{k_2 \varepsilon''_{LC}}{2\left(\varepsilon'_{LC} - sin^2\theta\right)^{1/2}} \right.$$
$$\left. \times \left(1 + tan^2\left(k_2 d \left(\varepsilon'_{LC} - sin^2\theta\right)^{1/2}\right)\right) \right] \tag{16}$$

$$L_{LC} = \frac{k_2}{\omega^2\varepsilon_0(\varepsilon'_{LC} - sin^2\theta)^{1/2}} \left[tan\left(k_2 d \left(\varepsilon'_{LC} - sin^2\theta\right)^{1/2}\right) \right] \tag{17}$$

TABLE I
EXTRACTED CORRECTION TERMS VERSUS RM DOPING
CONCENTRATION

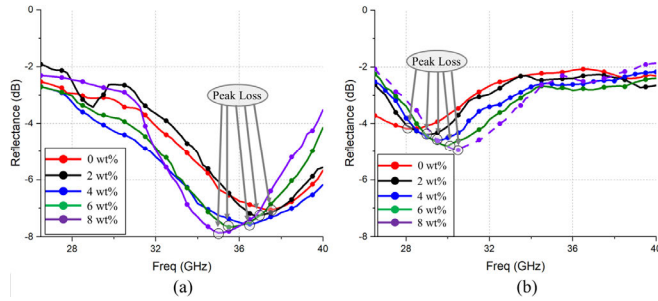| RM concentration (wt%)	Correction terms α ($\varepsilon_\parallel$)	β ($\varepsilon_\perp$)	Δ ($\delta_\perp$)	ξ ($\delta_\parallel$)
0	0	0	0	0.05
2	0.13	0.1	0.02	0.08
4	0.25	0.13	0.05	0.11
6	0.42	0.2	0.06	0.16
8	0.47	0.25	0.11	0.26

Fig. 10. Extracted (a) anisotropy and (b) loss tangent.

Fig. 9. Measured S_{11} versus the RM concentration for two extreme states. (a) Parallel alignment and (b) vertical alignment.

Fig. 11. (a) Schematic and (b) constructed EO evaluation system to obtain voltage-switching effective LC tilting angle (θ_{lc}) conditions and switching dynamics in PNLC cells.

RM doping weight percentage increased, the z-component of the permittivity tensor increased owing to polymerization. The effective permittivity changed to the average value between the RM and LC depending on the polymerized network density in the LC cavity. The calculated effective permittivity values at the resonance frequency versus the RM concentration from 2 to 8 wt% were 2.56, 2.59, 2.66, and 2.71, respectively. This is because the anisotropic permittivity of the doped RM was small along the extraordinary axis and large along the ordinary axis compared with that of the NLC. The loss tangent varied from 0.11 and 0.26 for the parallel and vertical alignments, respectively. The calculated values were obtained by setting the peak loss points as the resonance frequencies.

The extracted dielectric anisotropy and loss tangent versus the RM concentration are shown in Fig. 10. The solid and dashed lines represent the parallel and vertical alignments, respectively. As the RM concentration increased, the dielectric anisotropy changed from 1.1 to 0.39. The RM influenced the reconfigurability of the LC, and this phenomenon lowered the phase efficiency of the antenna. In addition, because of the high loss tangent, as shown in Fig. 10(b), antenna performance, such as efficiency, decreased. Despite establishing an RM network to enhance the switching dynamics, optimization of the RM concentrations was necessarily required. Accordingly, the exact characterization of the selected material should be performed to employ these materials in the design of RAs.

C. Field On/Off Time and Bias Voltage Evaluation

In the PNLC cells prepared with different RM network density conditions, the bias-dependent switching of the effective dielectric (ε_{eff}) values in the RF regime and its switching dynamics were evaluated from the electrooptic (EO) char-
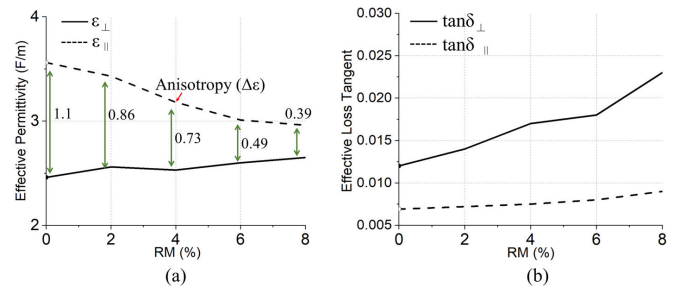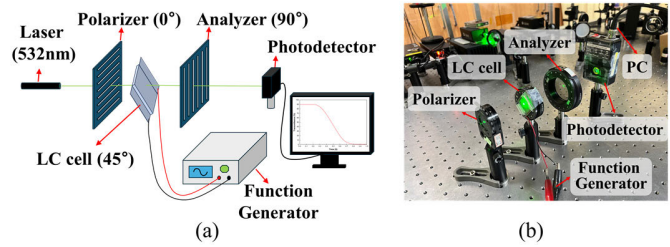
acterizations, as shown in Fig. 11. For this characterization, optically transparent LC cells with the RM-stabilized polymeric networks were fabricated by utilizing ITO-deposited glass cells with the same LC cell gap condition (10 μm) as the 1×2 RA LC cells. A function generator (33500 B, Keysight) was utilized to operate the PNLC cell, a linear polarizer with an optical transmission axis set at $0°$ was placed before the PNLC cell, and another linear polarizer (analyzer) with an orthogonal transmission axis was placed behind the PNLC cell to evaluate the field-dependent effective tilting angle condition of the RM-stabilized LC layer from the retardation changes with the EO characteristics. The 532 nm laser (Cobolt Samba, HÜBNER Photonics) light source sequentially passed through the $0°$-linear polarizer, the PNLC cell that was rotated by $45°$ as the LC alignment direction, and the $90°$-analyzer to reach the photodetector (Model 2031, Newport). Because the effective refractive index anisotropy (Δn_{eff}(V)) and resultant optical retardation ($\Delta\Gamma_{eff}$(V)) inside the PNLC cell changed depending on the voltage conditions applied to the PNLC cell, the voltage-dependent effective tilting condition (θ_{lc}(V)) of the field-reoriented LC directors could be evaluated.

The optically characterized voltage-transmittance (V–T) curves of PNLC cells, prepared under two different RM concentrations of 0 and 8 wt% are shown in Fig. 12. The voltage bias region from 0 to 10 V, exhibiting abrupt director changes, was more precisely measured with a 1 mV step, and the bias region from 10 to 20 V was measured with a 15 mV bias step utilizing a $15\times$ voltage amplifier. As shown in (23), the V–T curves in the optical regime showed more oscillation peaks or valleys before saturation, approaching zero retardation with an increasing bias voltage condition when the range of the bias-switchable effective retardation ($\Delta\Gamma_{eff}$(V)) was larger, as shown in Fig. 12(a) obtained with the pristine LC cell compared with that of Fig. 12(b) obtained with the
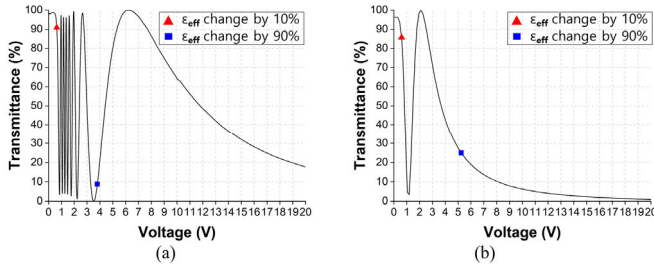
Fig. 12. Voltage-transmittance curves of the pristine LC and PNLC cells, prepared by utilizing RM concentrations of (a) 0 wt% and (b) 8 wt%.
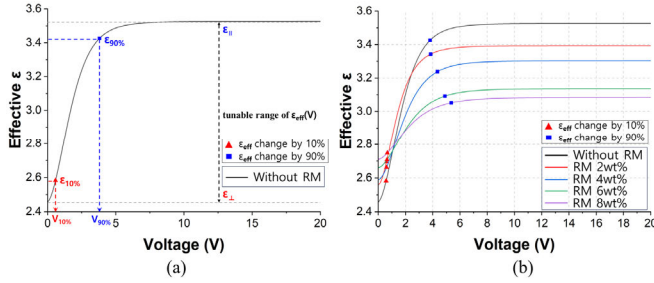

Fig. 13. Characteristics of LCs in the RF regime on voltage-dependent effective permittivity change according to RM concentration. (a) Pristine LC cell without RM network (0 wt% of RM doping concentration) and (b) PNLC with the RM network (8 wt% of RM doping concentration).

8 wt%-RM-doped PNLC cell

$$T(\%) = \sin^2\left(\frac{\Gamma_{eff}(V)}{2}\right) = \sin^2\left(\frac{\pi \Delta n_{eff}(V)d}{\lambda}\right) \quad (23)$$

where d is the cell gap of the pure LC or PNLC cell and λ is the wavelength of the light source utilized for EO characterization.

Using the results of the V–T measurements shown in Fig. 12, the $\Delta\Gamma_{eff}(V)$ sets were derived after the phase unwrapping. Thus, the voltage-dependent data analysis sets of $\Delta n_{eff}(V)$ and, consequently, $\theta_{lc}(V)$ could be analyzed using the following equation:

$$\Delta n_{eff}(V) = n_{eff}(V) - n_o$$
$$= \frac{n_e n_o}{\sqrt{n_e^2 \sin^2(\theta_{lc}) + n_o^2 \cos^2(\theta_{lc})}} - n_o. \quad (24)$$

Using the $\theta_{lc}(V)$ information derived from the EO characterization, the effective permittivity changes ($\varepsilon_{eff}(V)$) in the RF regime of the PNLC cells prepared with different RM concentrations can be evaluated using (25), as shown in Fig. 13. The permittivity values, after applying the extracted correction terms listed in Table I, were utilized for different RM concentration conditions

$$\varepsilon_{eff}(V) = \frac{\varepsilon_\perp \varepsilon_\parallel}{\sqrt{\varepsilon_\perp^2 \sin^2(\theta_{lc}) + \varepsilon_\parallel^2 \cos^2(\theta_{lc})}}. \quad (25)$$

Within the voltage-variable $\varepsilon_{eff}(V)$ ranges, different from the RM concentration conditions (varying from 0 to 8 wt%), as shown in Fig. 13, the bias voltage conditions for the effective permittivity changes of 10% and 90% were determined, and those conditions are marked in the graph as red triangles and blue squares, respectively. Effective permittivity

TABLE II
COMPARISON OF STUDIES ON CHARACTERIZATION OF PNLC AT THE mmWAVE BAND

Ref. Features	[17]	This Work
Freq. (GHz)	100	35.5
Material	PNLC	NLC/PNLC
Extraction of Loss Tangent	N.A.	Available
Bias Level	160V	0V*
Meas. Field-on	12ms	27.9ms
Meas. Field-off	210ms	56.4ms
RM Concentration	20%	0~8%
Transparent Electrode	N.A.	ITO
Thickness	45μm	10μm

*This study established two extreme phase states of the PNLC by pre-aligning.

change points with 10% and 90% variations were employed to characterize the field-on and field-off switching dynamics of the RM-stabilized PNLC cells in the RF operation regime. With precise V–T curve measurements, the transmittance level points corresponding to the effective permittivity changes with 10% and 90% variation could be marked with the same symbols as the red triangles and blue squares indicated in Fig. 12, even at the highly oscillating V–T curves owing to the relatively large optical anisotropy of LCs developed for RF applications.

The field-switching dynamic transmittance curves were measured for the PNLC cells prepared at different RM concentrations by connecting the photodetector signals to an oscilloscope (DSO1052B, Keysight) as shown in Fig. 14. With the transmittance-level information required to evaluate the switching response times based on the effective permittivity changes in the RF regime shown in Figs. 12 and 13, the time intervals corresponding to the field-on and field-off RF response times were analyzed, as shown in Fig. 14.

The field-on and field-off switching times (τ_{on} and τ_{off}, respectively) characterized by the effective permittivity changes in the RF regime, are summarized in Fig. 15. Because of the sample rate limitation in our oscilloscope measurements, some data points were missing in the periods exhibiting fast LC reorientation dynamics in Fig. 14, but the evaluation time points required for the field-on or field-off switching times could be precisely determined from the static EO measurements of the oscillatory V–T curve behaviors shown in Fig. 12. The switching times for the pristine LC cell without the RM network are $\tau_{on} = 1.25$ ms and $\tau_{off} = 594.1$ ms, respectively. As the RM network density increased with more RM doping concentration for the PNLC cell preparation, the switching times of τ_{on} slightly increased. This may be attributed to the decreasing behavior of the dielectric anisotropy that is highly related to the reduced dielectric torque for field-induced LC reorientation dynamics. At an RM concentration of 8 wt%, the field-on switching time (τ_{on}) of the PNLC cell was 27.9 ms.
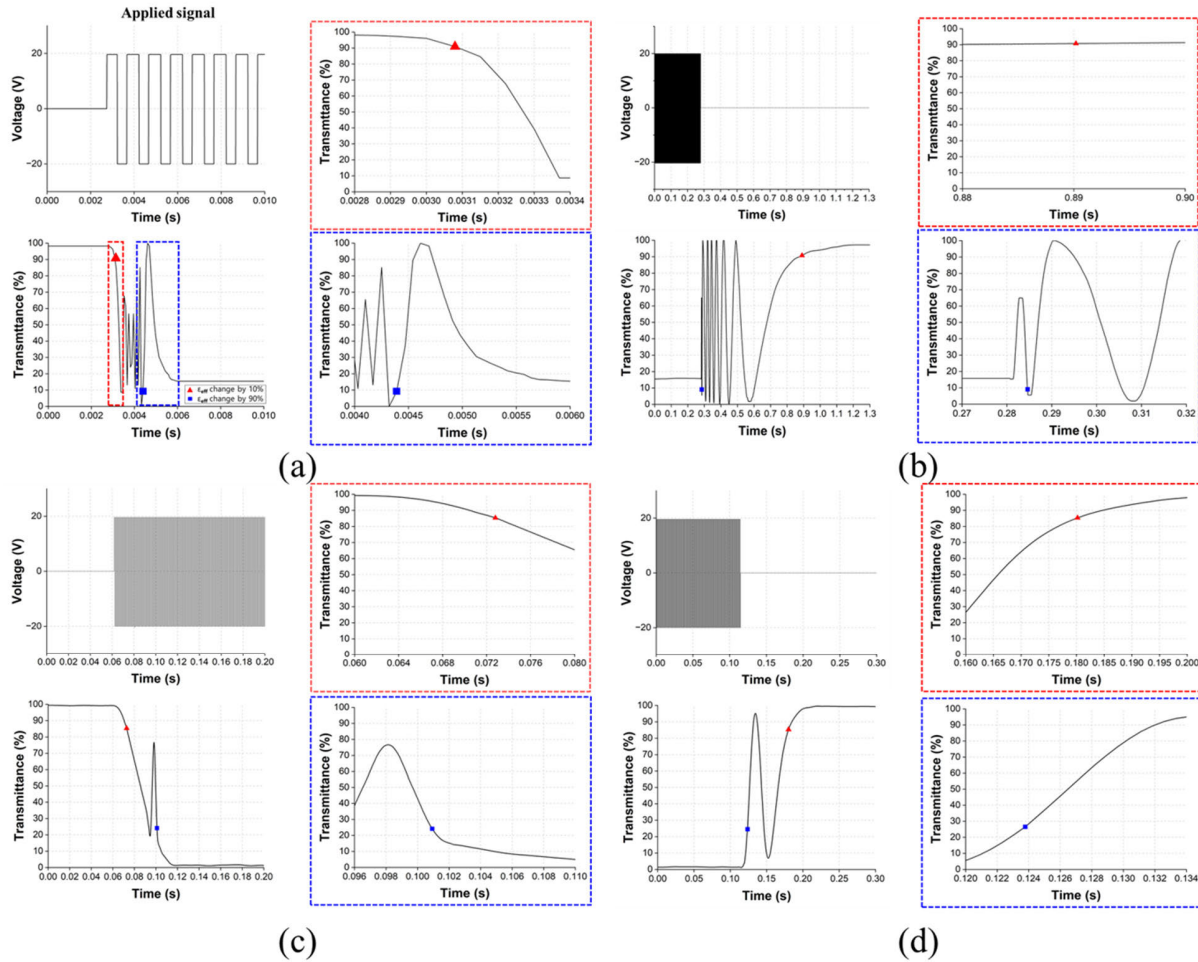
Fig. 14. Switching curves of pristine LC and PNLC cells (RM concentration of 8 wt%) and their applied signal conditions. (a) and (b) are the field-on and field-off switching curves for the pristine LC cell. (c) and (d) are the field-on and field-off switching curves for the PNLC cell.
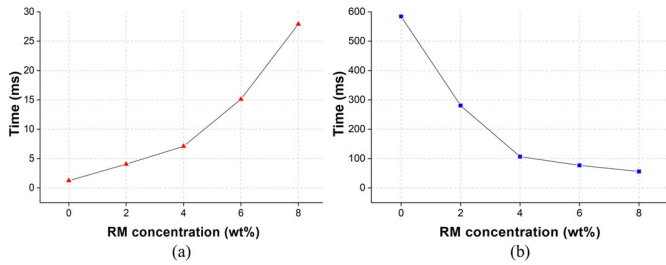

Fig. 15. (a) Field-on switching time and (b) field-off switching time according to the RM concentration of the PNLC cell, characterized by the effective permittivity changes in the RF regime.

On the other hand, the field-off switching time, τ_{off} can be considerably improved with an increase in RM network density; τ_{off} of 56.4 ms was achieved at an RM concentration of 8 wt%, which is over ten times faster than that of the pristine LC cell. RM-stabilized LC anchoring conditions uniformly distributed within the entire LC bulk layer could provide an effective method for improving the switching dynamics for LC-based RF device applications.

Table II presents a comparison of studies on the characterization of PNLC at the mmWave band. This article is the

first one to extract the complex permittivity of the PNLC through the establishment of a closed-form characterization. The proposed AUT does not require a bias circuit to achieve two extreme phase states, owing to its prealigned layers. Additionally, transparent electrodes enable successful UV exposure, leading to various concentrations of the RM.

IV. CONCLUSION

This study proposed a novel method for the exact characterization of anisotropic PNLC for reconfigurable RF devices in the mmWave band by employing a WG. For the first time, the complex permittivity of the PNLC has been extracted at the mmWave band. The proposed method is suitable owing to its simplicity and accuracy. A closed-form characterization can be achieved by designing a 1×2 RA cell, establishing an EQ, and choosing a WG corresponding to the claimed band. Finally, this study extracted the constitutive parameters of the PNLC at the Ka-band versus the RM concentration from 0 to 8 wt% and analyzed those mixtures in terms of dynamic speed and bias voltage. Promisingly, the proposed method could be applied to extract the electrical parameters of anisotropic materials, not only pristine LC or PNLC.

REFERENCES

[1] H.-Y. Wu, C.-F. Hsieh, T.-T. Tang, R.-P. Pan, and C.-L. Pan, "Electrically tunable room-temperature 2π liquid crystal terahertz phase shifter," *IEEE Photon. Technol. Lett.*, vol. 18, no. 14, pp. 1488–1490, Jul. 5, 2006, doi: 10.1109/LPT.2006.877579.

[2] H. Kim, J. Kim, and J. Oh, "Liquid-crystal-based X-band reactively loaded reflectarray unit cell to reduce reflection loss," *IEEE Antennas Wireless Propag. Lett.*, vol. 20, pp. 1898–1902, 2021.

[3] Q. Wang, Z. Su, S. Li, Y. Su, H. Zhao, and X. Yin, "Electrically tunable phase shifter with improved phase-shifting capability based on liquid crystal," *IEEE Microw. Wireless Technol. Lett.*, vol. 33, no. 5, pp. 527–530, May 2023.

[4] H. Kim, J. Kim, and J. Oh, "A novel systematic design of high-aperture-efficiency 2D beam-scanning liquid-crystal embedded reflectarray antenna for 6G FR3 and radar applications," *IEEE Trans. Antennas Propag.*, vol. 20, no. 10, pp. 1898–1902, Oct. 2021.

[5] S. Bildik, S. Dieter, C. Fritzsch, W. Menzel, and R. Jakoby, "Reconfigurable folded reflectarray antenna based upon liquid crystal technology," *IEEE Trans. Antennas Propag.*, vol. 63, no. 1, pp. 122–132, Jan. 2015.

[6] A. Alex-Amor, Á. Palomares-Caballero, A. Palomares, A. Tamayo-Domínguez, J. M. Fernández-González, and P. Padilla, "Generalized director approach for liquid-crystal-based reconfigurable RF devices," *IEEE Microw. Wireless Compon. Lett.*, vol. 29, no. 10, pp. 634–637, Oct. 2019.

[7] H. Kianmehr and R. R. Mansour, "Silicon-micromachined liquid crystal variable capacitors for tunable RF devices," in *IEEE MTT-S Int. Microw. Symp. Dig.*, San Diego, CA, USA, Jun. 2023, pp. 1058–1060.

[8] Y. Youn et al., "Liquid-crystal-driven reconfigurable intelligent surface with cognitive sensors for self-sustainable operation," *IEEE Trans. Antennas Propag.*, vol. 71, no. 12, pp. 9415–9423, Dec. 2023.

[9] J. Kim and J. Oh, "Liquid-Crystal-Embedded aperture-coupled microstrip antenna for 5G applications," *IEEE Antennas Wireless Propag. Lett.*, vol. 19, pp. 1958–1962, 2020.

[10] G. Perez-Palomino et al., "Design and experimental validation of liquid crystal-based reconfigurable reflectarray elements with improved bandwidth in F-band," *IEEE Trans. Antennas Propag.*, vol. 61, no. 4, pp. 1704–1713, Apr. 2013.

[11] M. W. Geis, T. M. Lyszczarz, R. M. Osgood, and B. R. Kimball, "30 to 50 ns liquid-crystal optical switches," *Opt. Exp.*, vol. 18, no. 18, p. 18886, 2010.

[12] G. Perez-Palomino et al., "Design and demonstration of an electronically scanned reflectarray antenna at 100 GHz using multiresonant cells based on liquid crystals," *IEEE Trans. Antennas Propag.*, vol. 63, no. 8, pp. 3722–3727, Aug. 2015.

[13] E. Doumanis et al., "Nematic liquid crystals for reconfigurable millimeter wavelength antenna technology," in *Proc. 7th Eur. Conf. Antennas Propag. (EuCAP)*, Apr. 2013, pp. 1791–1792.

[14] W. Zhang, Y. Li, and Z. Zhang, "A reconfigurable reflectarray antenna with an 8 μm-thick layer of liquid crystal," *IEEE Trans. Antennas Propag.*, vol. 70, no. 4, pp. 2770–2778, Apr. 2022.

[15] H. Kim and S. Nam, "Performance improvement of LC-based beam-steering leaky-wave holographic antenna using decoupling structure," *IEEE Trans. Antennas Propag.*, vol. 70, no. 4, pp. 2431–2438, Apr. 2022.

[16] D. C. Zografopoulos and R. Beccherelli, "Tunable terahertz fishnet metamaterials based on thin nematic liquid crystal layers for fast switching," *Sci. Rep.*, vol. 5, no. 1, p. 13137, Aug. 2015.

[17] R. Guirado, G. Perez-Palomino, M. Caño-García, M. A. Geday, and E. Carrasco, "mm-wave metasurface unit cells achieving millisecond response through polymer network liquid crystals," *IEEE Access*, vol. 10, pp. 127928–127938, 2022.

[18] D. E. Schaub and D. R. Oliver, "A circular patch resonator for the measurement of microwave permittivity of nematic liquid crystal," *IEEE Trans. Microw. Theory Techn.*, vol. 59, no. 7, pp. 1855–1862, Jul. 2011.

[19] W. Hu et al., "Design and measurement of reconfigurable millimeter wave reflectarray cells with nematic liquid crystal," *IEEE Trans. Antennas Propag.*, vol. 56, no. 10, pp. 3112–3117, Oct. 2008.

[20] S. Bulja, D. Mirshekar-Syahkal, R. James, S. E. Day, and F. A. Fernández, "Measurement of dielectric properties of nematic liquid crystals at millimeter wavelength," *IEEE Trans. Microw. Theory Techn.*, vol. 58, no. 12, pp. 3493–3501, Dec. 2010.

[21] P. Deo, D. Mirshekar-Syahkal, L. Seddon, S. E. Day, and F. A. Fernández, "Microstrip device for broadband (15–65 GHz) measurement of dielectric properties of nematic liquid crystals," *IEEE Trans. Microw. Theory Techn.*, vol. 63, no. 4, pp. 1388–1398, Apr. 2015.

[22] S. Henthorn and K. L. Ford, "Tuneable polarisation agnostic reflectarray element at mmWave using polymer dispersed liquid crystal," in *Proc. 17th Eur. Conf. Antennas Propag. (EuCAP)*, Mar. 2023, pp. 1–4.

[23] R. James, F. A. Fernandez, S. E. Day, S. Bulja, and D. Mirshekar-Syahkal, "Accurate modeling for wideband characterization of nematic liquid crystals for microwave applications," *IEEE Trans. Microw. Theory Techn.*, vol. 57, no. 12, pp. 3293–3297, Dec. 2009.

[24] H. Kim, S. Oh, S. Bang, H. Yang, B. Kim, and J. Oh, "Independently polarization manipulable liquid-crystal-based reflective metasurface for 5G reflectarray and reconfigurable intelligent surface," *IEEE Trans. Antennas Propag.*, vol. 71, no. 8, pp. 6606–6616, Aug. 2023.

[25] J. Yang et al., "Fully electronically phase modulation of millimeter-wave via comb electrodes and liquid crystal," *IEEE Antennas Wireless Propag. Lett.*, vol. 20, pp. 342–345, 2021.

[26] X. Li, H. Sato, Y. Shibata, T. Ishinabe, H. Fujikake, and Q. Chen, "Development of beam steerable reflectarray with liquid crystal for both E-plane and H-plane," *IEEE Access*, vol. 10, pp. 26177–26185, 2022.

[27] R. Guirado, P. De la Rosa, G. Perez-Palomino, M. Caño-García, E. Carrasco, and X. Quintana, "Characterization and application of dual frequency liquid crystal mixtures in mm-wave reflectarray cells to improve their temporal response," *IEEE Trans. Antennas Propag.*, vol. 71, no. 8, pp. 6535–6545, Aug. 2023.

[28] P. K. Rai et al., "Isotropic-nematic phase transition of single-walled carbon nanotubes in strong acids," *J. Amer. Chem. Soc.*, vol. 128, no. 2, pp. 591–595, 2006.

[29] Y. Shin et al., "Optically isotropic liquid crystal mode templated by nanoporous breath figure membrane," *Adv. Mater. Interface*, vol. 9, no. 7, pp. 1–13, Jan. 2022.

[30] K.-I. Joo et al., "Light-field camera for fast switching of time-sequential two-dimensional and three-dimensional image capturing at video rate," *IEEE Trans. Ind. Electron.*, vol. 67, no. 8, pp. 6975–6985, Aug. 2020.

[31] P. Hannan and M. Balfour, "Simulation of a phased-array antenna in waveguide," *IEEE Trans. Antennas Propag.*, vol. AP-13, no. 3, pp. 342–353, May 1965.

[32] F. Costa and A. Monorchio, "Closed-form analysis of reflection losses in microstrip reflectarray antennas," *IEEE Trans. Antennas Propag.*, vol. 60, no. 10, pp. 4650–4660, Oct. 2012.

[33] O. Luukkonen et al., "Simple and accurate analytical model of planar grids and high-impedance surfaces comprising metal strips or patches," *IEEE Trans. Antennas Propag.*, vol. 56, no. 6, pp. 1624–1632, Jun. 2008.

[34] F. Costa, "A simple effective permittivity model for metasurfaces within multilayer stratified media," *IEEE Trans. Antennas Propag.*, vol. 69, no. 8, pp. 5148–5153, Aug. 2021.

[35] F. Costa, A. Monorchio, and G. Manara, "Efficient analysis of frequency-selective surfaces by a simple equivalent-circuit model," *IEEE Antennas Propag. Mag.*, vol. 54, no. 4, pp. 35–48, Aug. 2012.

[36] S. A. Tretyakov and C. R. Simovski, "Dynamic model of artificial reactive impedance surfaces," *J. Electromagn. Waves Appl.*, vol. 17, no. 1, pp. 131–145, Jan. 2003.

[37] T.-W. Kim, J.-S. Park, and S.-O. Park, "A theoretical model for resonant frequency and radiation pattern on rectangular microstrip patch antenna on liquid crystal substrate," *IEEE Trans. Antennas Propag.*, vol. 66, no. 9, pp. 4533–4540, Sep. 2018.

[38] M. Yazdanpanahi, S. Bulja, D. Mirshekar-Syahkal, R. James, S. E. Day, and F. A. Fernandez, "Measurement of dielectric constants of nematic liquid crystals at mm-wave frequencies using patch resonator," *IEEE Trans. Instrum. Meas.*, vol. 59, no. 12, pp. 3079–3085, Dec. 2010.

[39] B. A. Munk, *Frequency Selective Surfaces, Theory and Design*. Hoboken, NJ, USA: Wiley, 2000.

Hogyeom Kim (Graduate Student Member, IEEE) received the B.S. degree in electrical engineering from Inha University, Incheon, South Korea, in 2016. He is currently pursuing the integrated master's and Ph.D. degrees with Seoul National University, Seoul, South Korea.

He served in the Korean Army from 2016 to 2018. His current research interests include transmit/reflectarray antennas, reconfigurable intelligence surfaces for B5G/6G communication, and millimeter-wave radar systems and liquid-crystal material-based metasurface.

Jae-Won Lee (Graduate Student Member, IEEE) received the B.S. degree in electronics engineering from Kyungpook National University, Daegu, Republic of Korea, in 2018, where he is currently pursuing the Ph.D. degree with the School of Electronic and Electrical Engineering.

His current research interests include liquid crystal displays and optics for 3-D imaging and 3-D displays.

Hak-Rin Kim (Member, IEEE) received the B.S., M.S., and Ph.D. degrees in electrical engineering from Seoul National University, Seoul, Republic of Korea, in 1998, 2000, and 2005, respectively.

In 2007, he joined the School of Electronics Engineering, Kyungpook National University, Daegu, Republic of Korea, where he is a Professor with the Display/Organic Electronics Laboratory. He is the author of more than 100 SCI(E) papers in international journals. His current research interests include tunable photonics using liquid crystals, geometric phase holographic optics, organic-based EO devices, and optics for 3-D imaging and 3-D displays.

Junkai Wang (Graduate Student Member, IEEE) received the B.S. degree in electronics engineering from Kyungpook National University, Daegu, Republic of Korea, in 2022, where he is currently pursuing the M.S. degree with the School of Electronic and Electrical Engineering.

His current research interests include liquid crystal displays and liquid crystal antenna.

Jungsuek Oh (Senior Member, IEEE) received the B.S. and M.S. degrees from Seoul National University, Seoul, South Korea, in 2002 and 2007, respectively, and the Ph.D. degree from the University of Michigan, Ann Arbor, MI, USA, in 2012.

From 2007 to 2008, he was with Korea Telecom as a Hardware Research Engineer, working on the development of flexible RF devices. In 2012, he was a Post-Doctoral Research Fellow at the Radiation Laboratory, University of Michigan. From 2013 to 2014, he was a Staff RF Engineer with Samsung Research America, Dallas, TX, USA, working as a project leader for the 5G/millimeter-wave antenna system. From 2015 to 2018, he was a Faculty Member at the Department of Electronic Engineering, Inha University, Incheon, South Korea. He is currently an Assistant Professor with the School of Electrical and Computer Engineering, Seoul National University, Seoul, South Korea. He has published more than 40 technical journals and conference papers. His research interests include mmWave beam focusing/shaping techniques, antenna miniaturization for integrated systems, and radio propagation modeling for indoor scenarios.

Dr. Oh is a recipient of the 2011 Rackham Predoctoral Fellowship Award at the University of Michigan. He has served as a Technical Reviewer for IEEE TRANSACTIONS ON ANTENNAS AND PROPAGATION and IEEE ANTENNAS AND WIRELESS PROPAGATION LETTERS, among other journals. He has served as a TPC Member and as the Session Chair for IEEE AP-S/USNC-URSI and ISAP.

Min-Seok Kim (Student Member, IEEE) received the B.S. degree in physics from Kyungpook National University, Daegu, Republic of Korea, in 2024, where he is currently pursuing the M.S. degree with the School of Electronic and Electrical Engineering.

His current research interests include the application of liquid crystal, metasurface, and optics for 3-D imaging.